catalysts

MDPI

Article

Stable Nitrogen-Doped TiO_2 Sols with Enhanced Visible-Light Response and Surface Wettability for Air Purification

Shuwei Wang [1], Jinhua Liu [2], Weijie Liu [2], Yiting Jia [2], Ning Liu [2], Yifan Ren [2], Yanni Zhang [2], Jingjing Zhang [2], Peng Zhao [2], Zhanyong Gu [3], Feng Wang [4,*], Wenbin Cao [5], Zhanwu Ning [2,*] and Peng Sun [2,*]

[1] Research Institute of Highway Ministry of Transport, Beijing 100088, China
[2] Institute of Urban Safety and Environmental Science, Beijing Academy of Science and Technology, Beijing 100054, China
[3] Hebei Key Laboratory of Pharmaceutical Polymer Excipients, College of Chemical Engineering, Shijiazhuang University, Shijiazhuang 050035, China
[4] National Centre for Archaeology, Beijing 100013, China
[5] School of Materials Science and Engineering, University of Science and Technology Beijing, Beijing 100083, China
* Correspondence: wangfeng1911@126.com (F.W.); nzwu@163.com (Z.N.); ustbsunpeng@163.com (P.S.)

Abstract

Photocatalytic coatings that can be immobilized on outdoor surfaces provide a promising route for distributed and passive purification of atmospheric pollutants. The practical application requires not only visible-light photocatalytic activity but also stable dispersion, facile coating and favorable interfacial properties. In this work, N-doped TiO_2 (N-TiO_2) sols with different nominal doping contents were prepared through hydrothermal treatment of peroxotitanic acid precursors containing different amounts of urea at 130 °C for 4 h. All samples exhibited anatase phase, while the shifts in XRD and Raman peaks indicated nitrogen-doping-induced lattice distortion. The sols exhibited monomodal particle size distributions with average hydrodynamic diameters in the range of 20.13 nm to 27.07 nm, and the high absolute zeta potentials (>30 mV) demonstrated good dispersion stability. The XPS results confirmed that nitrogen atoms were introduced at interstitial sites with Ti-O-N bonds and increased the relative proportion of surface hydroxyl oxygen from 13.9% to 34.2%. Nitrogen doping improved the visible-light absorption by decreasing the bandgap from 3.06 eV to 2.81 eV and reduced the water contact angle of the sol-derived films from 24.0° to as low as 8.6°. Among all samples, 1.0N-TiO_2 exhibited the highest NO removal efficiency of 72.5% under visible-light irradiation and retained good stability over five photocatalytic cycles. These results demonstrate that moderate nitrogen doping can simultaneously regulate the colloidal, optical and interfacial properties of TiO_2 sols, making them promising coating materials for functionalization of building envelopes or other outdoor surfaces for air purification.

Keywords: TiO_2; nitrogen doping; sol; visible light photocatalytic activity; air purification

Check for updates

Academic Editors: Chiara Lo Porto and Roberto Comparelli

Received: 7 August 2026
Revised: 23 September 2026
Accepted: 24 September 2026
Published: 16 October 2026

Copyright: © 2026 by the authors. Licensee MDPI, Basel, Switzerland. This article is an open access article distributed under the terms and conditions of the Creative Commons Attribution (CC BY) license.

1. Introduction

Air pollution poses significant threats to human health, ecosystem stability and overall environmental quality [1,2]. Transportation, industrial production and other anthropogenic activities constitute widespread and dispersed pollution sources. Once released, pollutants further disperse in ambient air and generally occur at relatively low concentrations, making centralized collection and purification impractical [3,4]. Although source-control technologies can substantially reduce the release of pollutants, they primarily operate before or

during emission and therefore have limited capacity to directly remove pollutants that have already dispersed into ambient air [5]. Consequently, purification technologies which can deal with low-concentration pollutants in ambient air have attracted increasing attention.

Semiconductor photocatalysts can generate reactive oxygen species under light irradiation, thereby purifying the pollutants adsorbed on their surfaces and providing an effective approach to improve ambient air quality [6,7]. When immobilized on outdoor surfaces (building facades, roofs, noise barriers, etc.), photocatalysts can turn these widely available surfaces into distributed and passive air-purification interfaces that utilize natural sunlight without using additional artificial energy or treatment equipment [8,9]. In addition, some photocatalysts exhibit photoinduced hydrophilicity, which facilitates the removal of deposited contaminants and helps maintain the cleanliness of outdoor surfaces, thereby preserving their photocatalytic activity and surface functionality over extended service periods [10]. Therefore, photocatalysts that possess air-purification activity and surface hydrophilicity show great potential in ambient air purification.

Among the various photocatalysts, titanium dioxide (TiO_2) in particular has attracted considerable attention due to its high chemical stability, high biosafety, excellent photocorrosion resistance and low cost [11]. However, due to its wide bandgap, TiO_2 mainly absorbs ultraviolet light, which restricts its utilization of solar light and consequently lowers its photocatalytic activity under solar irradiation. Therefore, strategies for extending the light-response range of TiO_2 have been extensively investigated [12–14]. Various modification methods, including doping, semiconductor coupling and surface sensitization have been developed for this purpose [15–17]. Elemental doping can regulate the electronic structure of TiO_2, although excessive doping may introduce charge-carrier recombination centers [18]. Semiconductor coupling can broaden light absorption and facilitate charge separation through heterojunction formation, but requires careful control of the interfacial structure [14]. Surface sensitization enables visible-light absorption and electron injection into TiO_2, although the sensitizer may suffer from desorption or photodegradation [13]. Among these strategies, nitrogen doping is particularly attractive because N 2p-derived states can be introduced near or above the O 2p valence band, thereby extending the optical response of TiO_2 into the visible-light region [19]. In addition, nitrogen doping avoids the introduction of potentially toxic heavy-metal species, while urea is inexpensive and compatible with the aqueous hydrothermal synthesis route used in this study [18–20].

While intrinsic photocatalytic performance is essential, the physical form of a material and its method of application are also important considerations for practical use. TiO_2 photocatalysts are commonly prepared as nanopowders, which are prone to agglomeration and may pose a risk of dust release during handling and transfer. For use, the powders generally need to be redispersed; however, some agglomerates are difficult to fully deagglomerate, and the additional redispersion step increases both the complexity and cost of application [21,22]. In contrast, TiO_2 sols, namely colloidal dispersions of nanosized TiO_2 particles in water, can be directly applied to substrate surfaces by spraying, dip coating or brushing, facilitating uniform coverage over large areas and geometrically complex surfaces [23,24]. Nevertheless, the sols must maintain sufficient colloidal stability during storage and application to prevent particle aggregation and sedimentation [25]. Therefore, developing TiO_2 sols that combine good colloidal stability, visible-light responsiveness and surface hydrophilicity is important for outdoor air-purifying functional surfaces.

Herein, a series of N-TiO_2 sols with different doping concentrations were synthesized. The effects of nitrogen doping on the crystal phase, particle morphology, colloidal size distribution, colloidal stability, surface chemical states, optical absorption properties and surface wettability of the resulting films were systematically investigated. Nitric oxide (NO) was selected as a model atmospheric pollutant to evaluate the photocatalytic purification

performance under visible-light irradiation. And the cycling stability of the sol-derived coatings was also investigated. The novelty of this work lies in the development of stable N-TiO_2 sols that combine good colloidal stability, enhanced visible-light response, favorable surface wettability, and stable photocatalytic performance, thereby providing a readily applicable liquid-phase material for air-purification coatings.

2. Results and Discussion

2.1. Crystal Structure and Morphology

The XRD results of the N-TiO_2 samples are presented in Figure 1. All samples exhibited diffraction peaks located at approximately 25.3°, 37.8°, 48.0°, 53.9°, 55.0° and 62.7°, which can be attributed to the (101), (004), (200), (105), (211) and (204) crystal planes of standard anatase TiO_2 (JCPDS No. 21-1272), respectively [26]. Figure 1b presents an enlarged view of the (101) diffraction peaks of the samples. As shown in Figure 1b, the anatase (101) peak (2θ) was located at 25.34° for TiO_2 and shifted slightly to 25.32°, 25.27° and 25.26° for 0.5N-TiO_2, 1.0N-TiO_2 and 1.5N-TiO_2, respectively. According to Bragg's law, the shift in the (101) peak toward lower 2θ indicates a slight increase in the corresponding d_{101} interplanar spacing and suggests dopant-induced lattice distortion [27]. The direction of the diffraction-peak shift depends on the dopant species, ionic size, lattice position and the defects generated during doping. For example, Ag doping has been reported to shift the anatase (101) peak toward lower 2θ [28], whereas Zr doping resulted in a shift in the anatase diffraction peaks toward higher 2θ [29]. The average crystallite sizes estimated using the Scherrer equation were 12.30, 11.98, 11.33, and 10.97 nm for TiO_2, 0.5N-TiO_2, 1.0N-TiO_2, and 1.5N-TiO_2, respectively, indicating a slight decrease in crystallite size with increasing nominal nitrogen doping level.

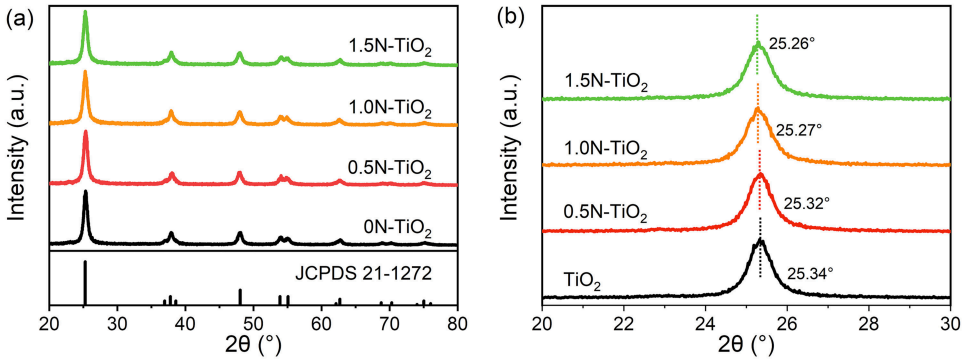


Figure 1. (**a**) XRD patterns; (**b**) enlarged (101) diffraction peaks of the as-prepared sol samples.

Figure 2a shows the Raman spectra of the as-prepared sol samples. The peaks located at about 148.2 cm^{-1}, 196.6 cm^{-1}, 390.4 cm^{-1}, 506.8 cm^{-1} and 629.2 cm^{-1} can be ascribed to E_g, E_g, B_{1g}, B_{1g}+A_{1g} and E_g of the standard anatase TiO_2 [30]. Figure 2b shows an enlarged view of the low-frequency E_g band at about 148.2 cm^{-1}, which shifts gradually to lower wavenumber (redshift) with increasing nominal nitrogen doping concentration. According to previous studies, Raman peak positions can be affected by crystallite-size effects, nonstoichiometric defects, and lattice strain [31,32]. In the present study, the average crystallite size calculated using the Scherrer equation decreased with increasing nitrogen-doping level. However, a decrease in the crystallite size of anatase TiO_2 generally causes a blue shift and broadening of the low-frequency E_g Raman mode because of the phonon-confinement effect [33], which is inconsistent with the redshift observed in this work. Therefore, the observed Raman redshift is unlikely to originate from the crystallite-size effect and may instead be mainly associated with nitrogen-induced nonstoichiometric defects, local lattice

strain, and changes in the Ti–O bonding environment, which may reduce the effective force constant of the Ti–O lattice vibrations and induce phonon softening [34].

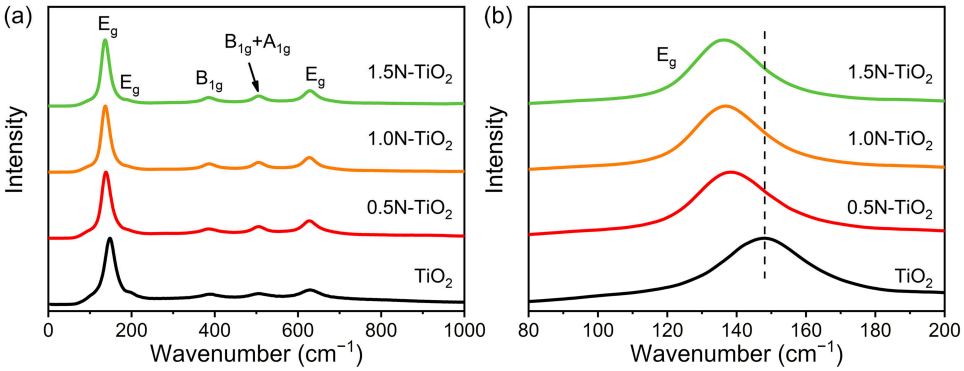


Figure 2. (**a**) The Raman spectra; (**b**) enlarged E_g of the as-prepared N-TiO_2 sols.

Figure 3 demonstrates the morphologies of TiO_2 and 1.0N-TiO_2 sol samples. As shown in Figure 3a,b, the TiO_2 sol sample exhibits an elongated rice-like morphology and the exposed crystalline interplanar spacing is about 0.353 nm, which is consistent with the (101) plane [35]. In 1.0N-TiO_2, the rice-like morphology is retained although it becomes shorter. Meanwhile, the lattice-fringe spacing remained nearly unchanged. By measuring the particles in TEM images, the size statistical results were obtained and are presented in Figure S1 and Table S1. The average particle length decreased from 20.67 ± 4.53 nm for TiO_2 to 16.87 ± 2.42 nm for 1.0N-TiO_2, while the average width remained nearly unchanged (11.14 ± 2.25 and 11.44 ± 2.26 nm, respectively). Accordingly, the average aspect ratio decreased from 1.86 to 1.47, indicating that nitrogen incorporation mainly reduced the particle elongation rather than the particle width. Similar changes in particle dimensions and morphology with increasing nitrogen content have also been reported for hydrothermally synthesized N-TiO_2. However, the detailed mechanism has not been fully clarified. Suwannaruang et al. attributed the reduction in particle size at higher nitrogen contents to enhanced nucleation and strain/stress-induced suppression of grain growth [36]. Han et al. proposed that carbonate ions generated from urea decomposition can stabilize the {001} facets by lowering their surface energy and thereby alter facet-dependent crystal growth [37], whereas Liu et al. suggested that NH^{4+} generated from urea decomposition may adsorb on the high-energy {001} facets and modify the oriented attachment behavior of anatase TiO_2 [38]. Therefore, the reduced aspect ratio observed in the present study may be associated with changes in the anisotropic growth behavior of TiO_2 induced by nitrogen-containing or urea-derived species during hydrothermal treatment.

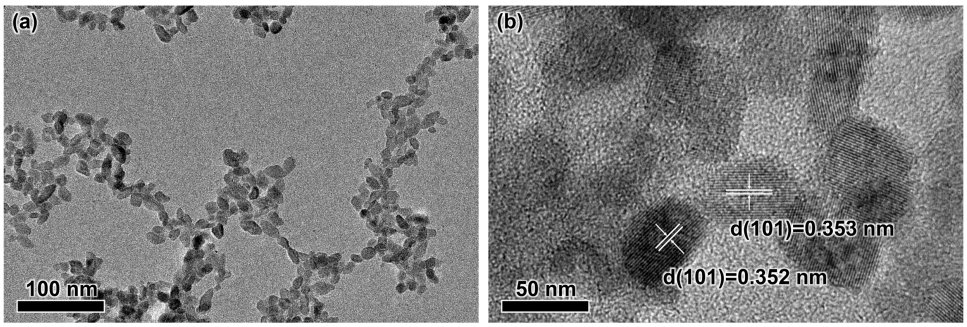


Figure 3. *Cont.*

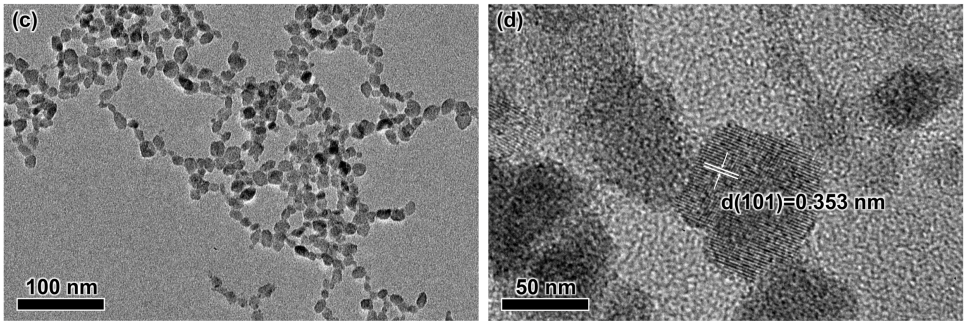


Figure 3. (**a**) TEM and (**b**) HRTEM of TiO_2 sol; (**c**) TEM and (**d**) HRTEM of 1.0N-TiO_2 sol.

Figure 4 presents the surface SEM images of the sol-derived TiO_2 and 1.0N-TiO_2 films. Both films exhibited similar and relatively uniform surface textures without obvious large-scale cracks. Since no organic additives, binders, pore-forming agents or structure-directing agents were introduced during film preparation, the observed porous surface morphology was mainly attributed to the natural deposition and packing of TiO_2 nanoparticles during drying.

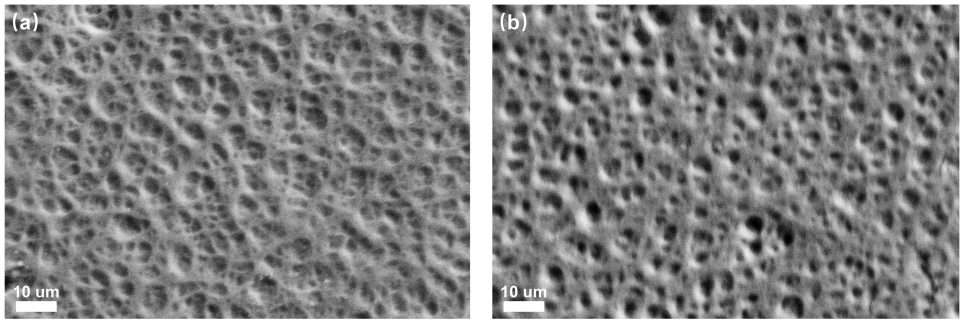


Figure 4. Surface SEM images of the sol-derived (**a**) TiO_2 and (**b**) 1.0N-TiO_2 films.

2.2. Colloidal Particle Size and Stability

Because the synthesized TiO_2 samples are aqueous sols, their hydrodynamic size distributions and colloidal stability were investigated. Figure 5 shows the hydrodynamic size distributions of the prepared sol samples and the results are summarized in Table 1. All samples exhibited unimodal distributions, indicating good dispersion of the prepared sol samples. The average particle size gradually decreased from 27.07 nm for TiO_2 sol to 20.13 nm for 1.5N-TiO_2 sol with the increasing nominal nitrogen doping concentration. The hydrodynamic diameters of TiO_2 and 1.0N-TiO_2 were comparable to the particle sizes estimated from the TEM images, suggesting limited particle aggregation in the aqueous sols. The polydispersity index (PDI) reflects the broadness of the hydrodynamic size distribution measured by DLS. Generally, a PDI value below 0.3 is considered indicative of a relatively narrow and homogeneous particle size distribution [39,40]. In this work, the PDI values ranged from 0.096 to 0.182, indicating relatively narrow and uniform hydrodynamic size distributions. As shown in Table 1, although the absolute zeta-potential values varied non-monotonically with the nominal nitrogen-doping level, all values were higher than 30 mV, indicating good colloidal stability [41,42]. This non-monotonic variation may result from the combined effects of changes in the surface hydroxyl groups, N-containing surface species and adsorbed ions on the surface charge and electrical double layer of the particles. A similar non-monotonic dependence on dopant concentration has been reported for catechin-capped Ag-doped TiO_2, suggesting that the zeta potential is not governed solely by the dopant concentration [43]. However, direct numerical comparison among different

systems should be made cautiously because zeta potential also depends on the dispersion medium, pH, ionic strength and particle concentration [44].

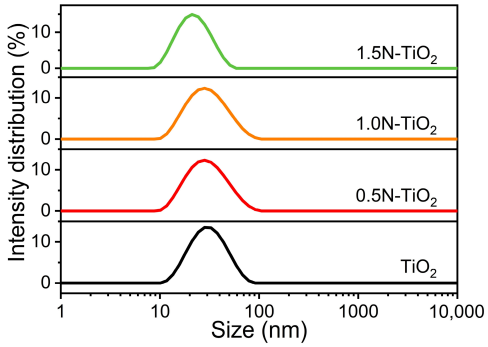


Figure 5. The size distribution of the as-prepared sol samples.

Table 1. The average size, zeta potential and PDI of as-prepared sol samples.

Samples	Average Size/nm	Zeta Potential/mV	PDI
TiO_2	27.07	−35.0	0.169
0.5N-TiO_2	26.69	−43.5	0.182
1.0N-TiO_2	22.30	−30.6	0.096
1.5N-TiO_2	20.13	−34.7	0.128

2.3. The Chemical States

The chemical states were investigated by XPS. Figure 6a shows the survey spectra of the samples. Ti, O and C signals were detected in all samples, together with N signals in N-TiO_2 samples. The C 1s peak was used for calibration at 284.6 eV. Figure 6b presents the high-resolution Ti 2p binding energy. The peaks located at about 464.4 eV and 458.7 eV can be ascribed to Ti $2p_{1/2}$ and Ti $2p_{3/2}$, respectively [45,46]. The splitting energy is 5.7 eV, indicating the valence state of Ti is +4 [45]. Compared with undoped TiO_2, the Ti 2p peaks of N-TiO_2 samples shifted toward lower binding energy, suggesting the increase in electron density around Ti atoms after nitrogen incorporation [47]. The direction of the Ti 2p binding-energy shift depends on the dopant species and the resulting local electronic environment of Ti. An increase in the electron density around Ti generally shifts the Ti 2p peaks toward lower binding energy, whereas a decrease in electron density generally leads to a shift toward higher binding energy. For example, Cu^{2+} doping has been reported to shift the Ti 2p peaks toward lower binding energy [12], whereas Se^{4+} doping resulted in a shift toward higher binding energy because of electron transfer from Ti to Se [48]. However, the magnitude of the shift is not fixed, because it also depends on the dopant concentration, lattice position, and local chemical environment. Figure 6c shows the high-resolution O 1s binding energy, which can be divided into two parts. The peak located at about 530.1 eV can be attributed to lattice oxygen (O_L), while the peak located at about 531.1 eV can be attributed to surface-adsorbed hydroxyl oxygen (O_A) [49,50]. The relative proportions of $O_A/(O_A+O_L)$ in TiO_2, 0.5N-TiO_2, 1.0N-TiO_2 and 1.5N-TiO_2 were 13.9%, 17.2%, 22.1% and 34.2%, respectively, indicating that nitrogen doping promoted the formation of O_A [51,52]. Surface hydroxyl groups play an important role in photocatalytic surface reactions by providing adsorption and reaction sites for pollutant molecules and reaction intermediates. They can also participate in the trapping of photogenerated holes and the formation of reactive oxygen species, thereby facilitating pollutant adsorption and photocatalytic oxidation [53]. The regulation of surface hydroxylation is not exclusive to nitrogen doping and depends strongly on the dopant species. For example, F modification has been reported to decrease the amount of surface hydroxyl groups [54], whereas Mo doping can promote

surface hydroxylation [55]. As shown in Figure 6d, the N-TiO_2 samples exhibited N 1s peaks centered at about 399.9 eV, which can be attributed to interstitial nitrogen of Ti-O-N structures [56]. The nitrogen contents of the N-TiO_2 samples are summarized in Table S2.

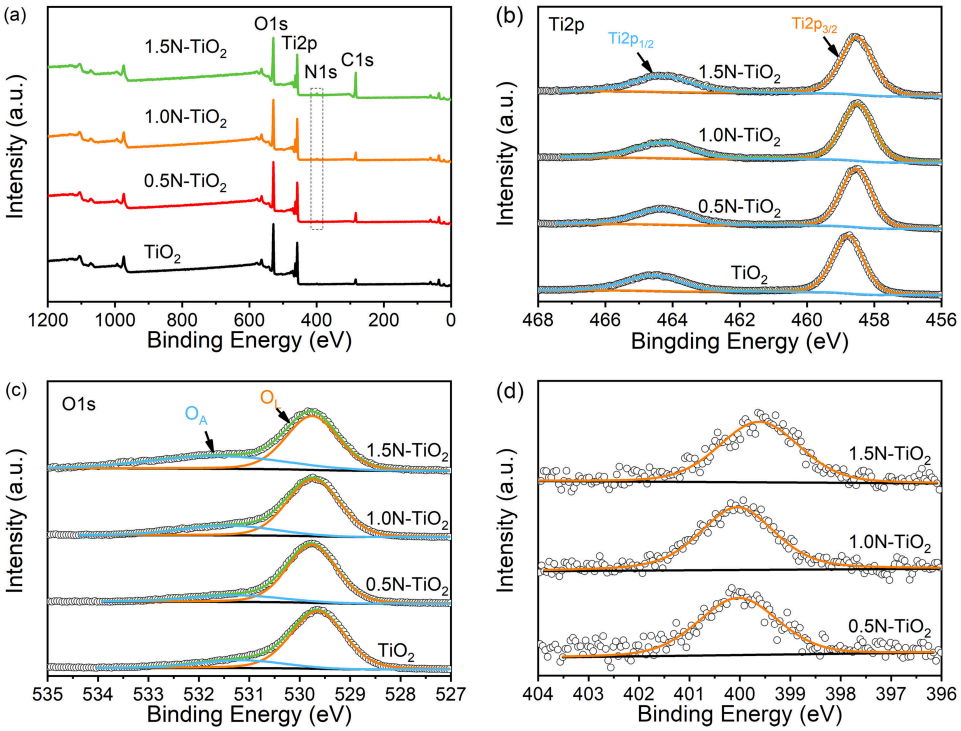


Figure 6. (**a**) Survey spectra, (**b**) high-resolution Ti 2p, and (**c**) high-resolution O 1s of all samples; (**d**) high-resolution N 1s of N-TiO_2 samples.

2.4. Optical Absorption and Band Structure

Figure 7a shows the UV-Vis absorption spectra of all samples in the range from 200 nm to 800 nm. The undoped TiO_2 exhibited absorption predominantly in the UV region, while N-TiO_2 samples exhibited enhanced absorption in the visible-light region from 400 nm to 500 nm and the absorption intensity increased with the increasing nitrogen doping concentration. The bandgap value (E_g) can be calculated by the Tauc equation (Equation (1)) [57,58]:

$$(\alpha h\upsilon)^{1/2} = B(h\upsilon - E_g) \quad (1)$$

where α is the absorption coefficient, h is Planck's constant, υ is the frequency of irradiated photons, and B is a proportionality constant. The E_g values can be obtained through measuring the intercepts of the tangents shown in Figure 7b. The results show that the E_g values gradually decreased from 3.06 eV for undoped TiO_2 to 2.81 eV for 1.5N-TiO_2 with increasing nitrogen doping concentration (Table 2). Correspondingly, the absorption edge shifted from 405.2 nm to 441.2 nm.

Figure 7c illustrates the valence band XPS spectra of the prepared samples. The valence band edges of TiO_2, 0.5N-TiO_2, 1.0N-TiO_2 and 1.5N-TiO_2 were 2.86, 2.70, 2.73 and 2.69 eV, respectively. Compared with undoped TiO_2, the valence-band edges of the N-TiO_2 samples shifted toward lower binding energy, which may be attributed to the introduction of N-related states above the O 2p valence band [19,59]. Non-metal dopants may introduce p-derived states near the O 2p valence band, whereas transition-metal dopants may shift the band edges or introduce localized d states within the bandgap [18,60,61]. Therefore, the electronic-structure change observed here could be considered characteristic of the present N-TiO_2 system. Based on the optical bandgaps and valence band positions, the schematic

band structures of the samples are illustrated in Figure 7d, using TiO_2 and 1.5N-TiO_2 as examples.

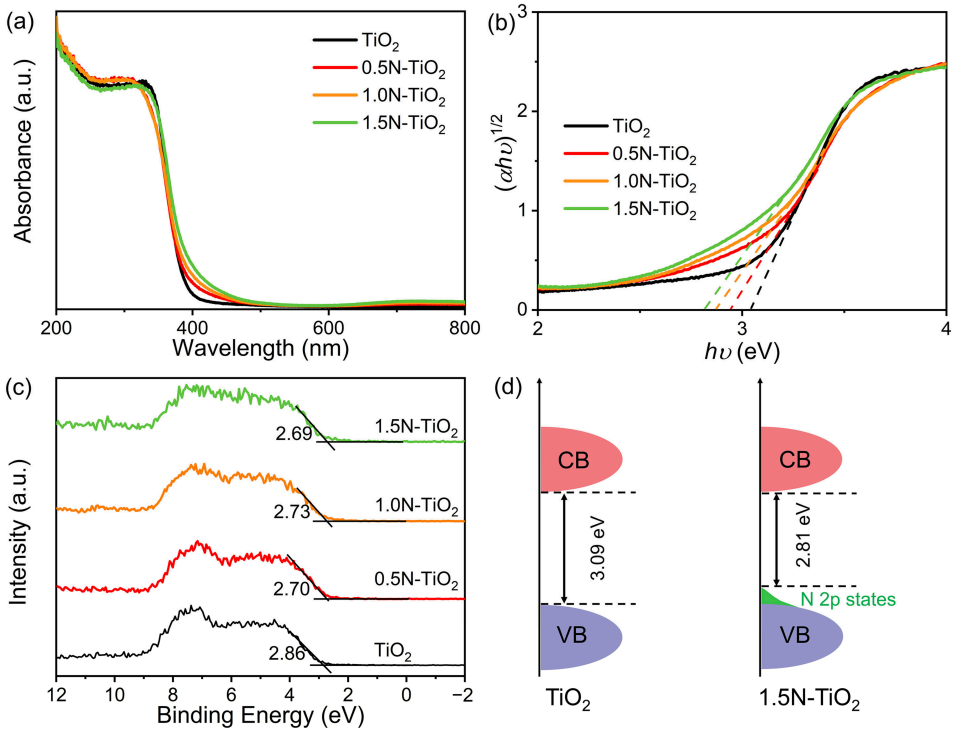


Figure 7. (**a**) UV-Vis absorption spectra, (**b**) Tauc plots, (**c**) valence band spectra of the prepared samples; (**d**) schematic band structures of TiO_2 and 1.5N-TiO_2. CB and VB denote the conduction band and valence band, respectively.

Table 2. Optical absorption edges and bandgaps of the as-prepared sol samples.

Samples	Absorption Edge/nm	Bandgap/eV
TiO_2	405.2	3.06
0.5N-TiO_2	421.8	2.94
1.0N-TiO_2	432.0	2.87
1.5N-TiO_2	441.2	2.81

2.5. The Wettability of Sol-Derived Films

The wettability of the films derived by the sol samples was evaluated by measuring their water contact angles, and the results are shown in Figure 8. The undoped TiO_2 sample prepared in this work exhibited a measured water contact angle of 24.0°. After nitrogen doping, the water contact angle decreased markedly. The contact angle of 0.5N-TiO_2 decreased to 13.6°, while those of 1.0N-TiO_2 and 1.5N-TiO_2 decreased to 9.3° and 8.6°, respectively. These results indicate that nitrogen doping effectively improves the hydrophilicity of TiO_2 sol-derived films. In particular, the contact angles of 1.0N-TiO_2 and 1.5N-TiO_2 were below 10°, suggesting the formation of superhydrophilic surfaces.

Similar improvements in surface wettability have also been reported for TiO_2 films containing other dopants. For example, a water contact angle of 5.1° was reported for a Cu-doped TiO_2 film [62]. Ahmad et al. reported water contact angles of 30°, 29°, 28° and 24° for undoped, Mg-doped, Ni-doped and Sn-doped TiO_2 films, respectively [63]. These comparisons indicate that nitrogen doping can also reduce the water contact angle of TiO_2 films to a relatively low level, thereby producing highly hydrophilic surfaces. Nevertheless, direct numerical comparison should be made cautiously because contact-angle values are

also affected by the dopant concentration, surface morphology, film preparation method, irradiation conditions and measurement procedure.

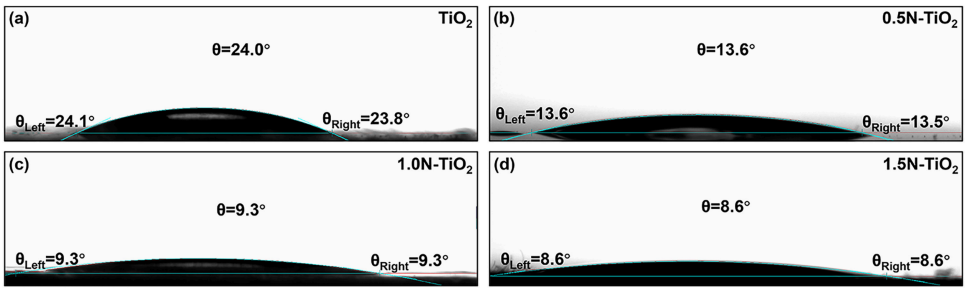


Figure 8. Water contact angles of sol-derived films. (**a**) TiO_2; (**b**) 0.5N-TiO_2; (**c**) 1.0N-TiO_2; (**d**) 1.5N-TiO_2.

The improved wettability of N-TiO_2 sol films can be attributed to a synergistic effect between the surface chemical environment and photoinduced hydrophilicity. As shown in the XPS results, the O 1s spectra confirmed that N doping promoted the formation of surface-adsorbed hydroxyl groups, which can act as adsorption sites for water molecules and promote the spreading of water droplets on the film surface [64]. On the other hand, nitrogen doping narrows the bandgap and enhances the visible-light absorption ability of TiO_2. The enhanced light absorption promotes the generation and migration of photoinduced holes to the surface, converting bridging oxygen species into surface hydroxyl groups and further strengthening the photoinduced hydrophilicity [65,66]. Such a synergistic effect is not exclusive to nitrogen doping, since other dopants, such as Fe and Bi, have also been reported to regulate the hydrophilicity and photoinduced wetting behavior of TiO_2 films [10,67].

2.6. Photocatalytic NO Purification Activities

The photocatalytic NO purification activities of the sol-derived films were evaluated and the results are shown in Figure 9. As shown in Figure 9a, undoped TiO_2 exhibited low NO purification efficiency (<10%), which can be attributed to its limited absorption in the visible-light region. In contrast, all N-TiO_2 samples showed markedly enhanced NO purification performance. The photocatalytic activities of all samples followed the order TiO_2 < 0.5N-TiO_2 < 1.5N-TiO_2 < 1.0N-TiO_2, and the highest NO purification efficiency was 72.5% (1.0N-TiO_2). Although 1.5N-TiO_2 exhibited the strongest visible-light absorption, its NO purification efficiency was lower than that of 1.0N-TiO_2, indicating that photocatalytic activity was not determined solely by optical absorption [68]. Excessive nitrogen doping may introduce defect states that can act as recombination centers of photoinduced electrons and holes [69]. Similar concentration-dependent effects have been reported for Ni-doped and Fe-doped TiO_2, in which photocatalytic activity decreased when the doping concentration exceeded the optimal level [70,71]. Consequently, 1.0N-TiO_2 exhibited the optimal balance between visible-light absorption and charge carriers' separation. The dark adsorption test was also performed using the optimal 1.0N-TiO_2 film. As shown in Figure S2, the outlet NO concentration gradually returned to and stabilized at approximately 1 ppm within 30 min under dark conditions. This result indicates that adsorption–desorption equilibrium had been established before irradiation. Therefore, the decrease in NO concentration observed after the light was turned on was attributed to the photocatalytic reaction. A small amount of NO_2 was detected during the photocatalytic reaction over 1.0N-TiO_2, and its concentration remained at approximately 0.01 ppm after the initial fluctuation (Figure S3). Despite differences in the reaction conditions, the NO purification efficiency of 1.0N-TiO_2 was relatively high compared with those of other modified TiO_2 photocatalysts

reported in the literature (Table S3). Figure 9b shows the cycling photocatalytic performance of 1.0N-TiO_2 over five consecutive cycles. The NO purification efficiency remained nearly unchanged during the five cycles, indicating good stability of the 1.0N-TiO_2 sol sample.

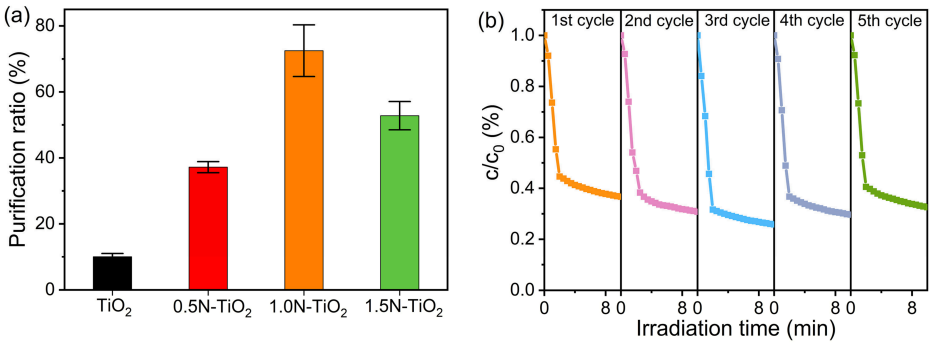


Figure 9. (**a**) NO purification activities of as-prepared sol samples, (**b**) the recycling test results of 1.0N-TiO_2.

Based on the above results, the proposed mechanism for the enhanced visible-light photocatalytic NO removal and surface hydrophilicity of N-TiO_2 is illustrated in Figure 10. The experimental results indicate that nitrogen was mainly incorporated as interstitial Ti-O-N species and increased the relative proportion of surface hydroxyl oxygen. The optical and valence-band results suggest that N-related electronic states were introduced above the O 2p valence band, thereby decreasing the optical bandgap and extending the light-response range of TiO_2 into the visible region. Under visible-light irradiation, the photogenerated charge carriers may participate in surface redox reactions and generate reactive oxygen species, thereby promoting the oxidation and removal of adsorbed NO.

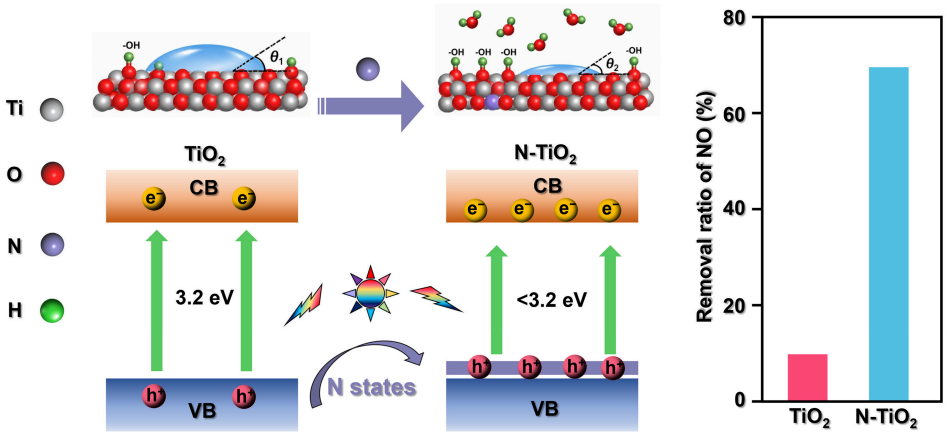


Figure 10. Proposed mechanism for visible-light photocatalytic NO removal and enhanced surface hydrophilicity of N-TiO_2.

In addition, the increased proportion of surface hydroxyl species provides more sites for water adsorption and facilitates the spreading of water droplets, accounting for the decrease in water contact angle after nitrogen doping. Enhanced visible-light absorption may also facilitate photoinduced surface hydroxylation and further improve the wettability of the films. Although 1.5N-TiO_2 exhibited stronger visible-light absorption and a higher proportion of surface hydroxyl species, its photocatalytic activity was lower than that of 1.0N-TiO_2. This result suggests that excessive nitrogen incorporation may introduce defect states that promote charge-carrier recombination [72,73]. Therefore, the optimal performance of 1.0N-TiO_2 may be attributed to a balance among visible-light harvesting, charge-carrier utilization and surface reaction properties.

3. Materials and Methods

3.1. Materials

Titanium oxysulfate ($TiOSO_4 \cdot 2H_2O$, >93%) was bought from Dandong Chemical Reagent Factory, Dandong, China. Ammonia solution ($NH_3 \cdot H_2O$, >28%), hydrogen peroxide (H_2O_2, >30%) and urea ($CO(NH_2)_2$, >99%) were bought from Shanghai Aladdin Biochemical Technology Co., Ltd, Shanghai, China. All commercially available chemicals were used directly without any further treatment, such as purification, drying or distillation. In our work, $TiOSO_4 \cdot 2H_2O$ was used as the titanium source, and $NH_3 \cdot H_2O$ was employed as the precipitating agent; H_2O_2 was then used to form the peroxotitanic acid, while urea was introduced as the nitrogen source.

3.2. Preparation

Firstly, 294 g of $TiOSO_4 \cdot 2H_2O$ was dissolved into 5 L of deionized water to obtain a titanium ion solution. Then, $NH_3 \cdot H_2O$ was added into titanium ion solution until the pH value reached 7. The mixture was stirred for 60 min at a stirring speed of 400 rpm and white precipitate appeared. Then, the mixture was washed by a centrifugation machine to obtain white titanium hydroxide precipitate. The purified white titanium hydroxide precipitate was added into 14 L of deionized water and heated to 40 °C, and then 1 L of H_2O_2 and 15 g of urea were added into it. After stirring for 1 h, the nitrogen-doped peroxotitanic acid was obtained. Then, this nitrogen-doped peroxotitanic acid was transferred into a stainless steel high-pressure reactor, heated to 130 °C and then maintained for 4 h. After the hydrothermal reaction, nitrogen-doped titanium dioxide (N-TiO_2) colloidal sol was obtained and denoted as 1.0N-TiO_2, where 1.0 represents the initial urea concentration of 1.0 g/L. Following the same method, 0.5N-TiO_2 and 1.5N-TiO_2 were prepared by using 7.5 g of urea and 22.5 g of urea, respectively. And the undoped TiO_2 sample was prepared without urea and named TiO_2.

3.3. Characterization

The obtained sol samples were dried at 65 °C for 24 h and ground to obtain solid powders. The crystal phase composition of the samples was tested by using an X-ray diffractometer (D8 ADVANCE, fabricated by Bruker Co., Ltd., Billerica, MA, USA) with a Cu target and a testing angle ranging from 10° to 80°. The Raman spectra of the samples were tested using a Raman spectrometer (RAM-500 DESEII, fabricated by JASCO Corporation, Hachioji, Tokyo, Japan) with a laser wavelength of 532 nm. The elemental composition and valence state of the sample were characterized using an X-ray photoelectron spectrometer (Escalab 250, fabricated by Thermo Fisher Scientific, Waltham, MA, USA). The optical absorption ability of the samples to visible light was characterized by using an ultraviolet–visible spectrophotometer (TU1901, fabricated by Beijing Purkinje General Instrument Co., Ltd., Beijing, China) at wavelengths ranging from 200 nm to 800 nm. The colloidal particle size distribution and zeta potential of the aqueous sol samples were tested using a laser particle size analyzer (Zetasizer Nano ZS-90, fabricated by Malvern Instruments Co., Ltd., Malvern, Worcestershire, UK) without dilution or the addition of any other dispersion medium.

3.4. Photocatalytic Activity Measurement

The photocatalytic reaction system is illustrated in Figure 11. The sol was sprayed on ground glass substrate with a size of 70 mm × 40 mm and the coating mass was 14 mg. And the glass was dried at 60 °C for 1 h. Then, the glass was placed in the reactor. The inlet NO concentration was maintained at 1 ppm, while the total gas flow rate was set at 1000 mL min^{-1} by adjusting the flow rates of the NO standard gas, O_2, and N_2. Firstly, the

gas flowed through the reactor for 30 min to reach the adsorption–desorption equilibrium in the dark. Then, a xenon lamp (300 W, with a cutoff of 400–800 nm) was turned on and the optical power density on the glass surface was maintained at 100 mW/cm^2. The NO concentration was measured by using APNA-370, Horiba. The NO purification efficiency was calculated according to the following equation:

$$\eta = \frac{c_{in} - c_{out}}{c_{in}} \times 100\% \quad (2)$$

where η is the NO purification efficiency, c_{in} is the NO concentration at the inlet of the photocatalytic reactor, and c_{out} is the NO concentration at the outlet of the reactor.

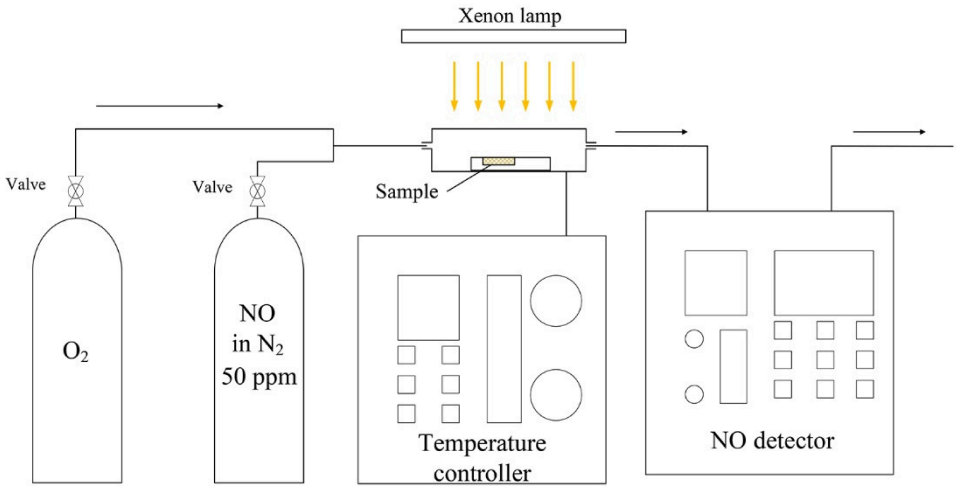


Figure 11. The photocatalytic reaction system.

For the cycling tests, the same 1.0N-TiO_2-coated substrate was reused throughout five consecutive photocatalytic cycles, and no freshly prepared coated substrate was used between cycles.

4. Conclusions

In summary, a series of N-TiO_2 sols with different doping concentrations were synthesized via a hydrothermal method using urea as the nitrogen source. Nitrogen doping preserved the anatase structure but induced local lattice distortion and reduced particle elongation. It also simultaneously regulated the electronic structure and surface chemical environment of TiO_2. Interstitial nitrogen extended the light-response range, while the progressive enrichment of surface hydroxyl species enhanced the wettability of the sol-derived films. The optimal 1.0N-TiO_2 sample achieved an NO purification efficiency of 72.5%, corresponding to a relative increase of 639% compared with undoped TiO_2, and maintained stable photocatalytic activity over five consecutive cycles. Beyond the improvement in photocatalytic performance, the products were obtained as stable and well-dispersed nanosols with narrow particle-size distributions. This liquid-phase form facilitates direct and uniform application onto large or geometrically complex substrates through simple coating processes, such as spraying, and avoids the additional redispersion procedures commonly required for photocatalyst powders. After immobilization, the combination of visible-light-responsive NO removal and favorable surface wettability may enable building facades, noise barriers and other outdoor structures to function as passive air-purifying and easier-to-clean surfaces under natural illumination.

Supplementary Materials: The following supporting information can be downloaded at https://www.mdpi.com/article/10.3390/catal16100916/s1, Figure S1: The (a1), (b1) length distribution and (a2), (b2) width distribution of TiO_2 and 1.0N-TiO_2 respectively; Figure S2: The adsorption–desorption equilibrium of NO for 1.0N-TiO_2 in the dark; Figure S3: NO and calculated NO_2 concentrations during photocatalytic NO removal over the 1.0N-TiO_2 sample under visible-light irradiation; Table S1: Particle dimensions and aspect ratios of TiO_2 and 1.0N-TiO_2 from TEM; Table S2: The elemental composition of as-prepared samples (atomic percentage); Table S3: The comparison of NO removal ability for different photocatalysts. References [70,71,74–83] are cited in the supplementary materials.

Author Contributions: Writing—original draft preparation, data curation, S.W. and P.S.; writing—review and editing, F.W., W.C., Z.N. and P.S.; data curation, formal analysis, J.L., W.L., Y.J. and N.L.; validation, Y.R., J.Z. and Z.G.; methodology, P.Z. and Y.Z. All authors have read and agreed to the published version of the manuscript.

Funding: This work was supported by the Science and Technology Special Program of Xicheng District of Beijing (XCKJZX-2025-32), the Beijing Natural Science Foundation (B2024106019), the Hebei Natural Science Foundation (B2024106019), and the Hebei Yanzhao Gold Platform Talent Recruitment and Development Initiative (A2025030).

Data Availability Statement: The data presented in this study are available upon request from the corresponding authors.

Conflicts of Interest: The authors declare no conflicts of interest.

References

1. Yang, S.; Li, M.; Guo, C.; Requia, W.J.; Sakhvidi, M.J.Z.; Lin, K.; Zhu, Q.; Chen, Z.; Cao, P.; Yang, L.; et al. Associations of long-term exposure to nitrogen oxides with all-cause and cause-specific mortality. *Nat. Commun.* **2025**, *16*, 1730. [CrossRef] [PubMed]
2. Tan, T.; Xu, X.; Gu, H.; Cao, L.; Liu, T.; Zhang, Y.; Wang, J.; Chen, M.; Li, H.; Ge, X. The Characteristics, Sources, and Health Risks of Volatile Organic Compounds in an Industrial Area of Nanjing. *Toxics* **2024**, *12*, 868. [CrossRef] [PubMed]
3. McDuffie, E.E.; Martin, R.V.; Spadaro, J.V.; Burnett, R.; Smith, S.J.; O'Rourke, P.; Hammer, M.S.; van Donkelaar, A.; Bindle, L.; Shah, V.; et al. Source sector and fuel contributions to ambient PM2.5 and attributable mortality across multiple spatial scales. *Nat. Commun.* **2021**, *12*, 3594. [CrossRef] [PubMed]
4. Chen, Y.; Rich, D.Q.; Masiol, M.; Hopke, P.K. Changes in ambient air pollutants in New York State from 2005 to 2019: Effects of policy implementations and economic and technological changes. *Atmos. Environ.* **2023**, *311*, 119996. [CrossRef]
5. Xiao, Z.; Yang, X.; Gu, H.; Hu, J.; Zhang, T.; Chen, J.; Pan, X.; Xiu, G.; Zhang, W.; Lin, M. Characterization and sources of volatile organic compounds (VOCs) during 2022 summer ozone pollution control in Shanghai, China. *Atmos. Environ.* **2024**, *327*, 120464. [CrossRef]
6. Morshedy, A.S.; El-Fawal, E.M.; Zaki, T.; El-Zahhar, A.A.; Alghamdi, M.M.; El Naggar, A.M.A. A review on heterogeneous photocatalytic materials: Mechanism, perspectives, and environmental and energy sustainability applications. *Inorg. Chem. Commun.* **2024**, *163*, 112307. [CrossRef]
7. Jabbar, Z.H.; Graimed, B.H. Recent developments in industrial organic degradation via semiconductor heterojunctions and the parameters affecting the photocatalytic process: A review study. *J. Water Process Eng.* **2022**, *47*, 102671. [CrossRef]
8. Khannyra, S.; Luna, M.; Gil, M.L.A.; Addou, M.; Mosquera, M.J. Self-cleaning durability assessment of TiO_2/SiO_2 photocatalysts coated concrete: Effect of indoor and outdoor conditions on the photocatalytic activity. *Build. Environ.* **2022**, *211*, 108743. [CrossRef]
9. Bersch, J.D.; Flores-Colen, I.; Masuero, A.B.; Dal Molin, D.C.C. Photocatalytic TiO_2-Based Coatings for Mortars on Facades: A Review of Efficiency, Durability, and Sustainability. *Buildings* **2023**, *13*, 186. [CrossRef]
10. Althamthami, M.; Guettaf Temam, E.; Temam, H.B.; Saad, R.; Hasan, G.G. Improved photocatalytic activity under the sunlight of high transparent hydrophilic Bi-doped TiO_2 thin-films. *J. Photochem. Photobiol. A Chem.* **2023**, *443*, 114818. [CrossRef]
11. Rajaram, P.; Jeice, A.R.; Jayakumar, K. Review of green synthesized TiO_2 nanoparticles for diverse applications. *Surf. Interfaces* **2023**, *39*, 102912. [CrossRef]
12. Mikaeili, F.; Rahaman, M.M.; Gouma, P.I. 3D Self-Supported Visible Light Photochemical Nanocatalysts. *Adv. Sci.* **2025**, *12*, 2502981. [CrossRef] [PubMed]
13. Ekanayake, S.A.; Mai, H.; Mahasivam, S.; Lu, J.; Wen, X.; Chen, D.; Caruso, R.A. Nitrogen-Rich Carbon Nanodot-Sensitized TiO_2 with MWCNT Composites for Efficient Visible Light Photocatalysis. *Adv. Mater. Interfaces* **2024**, *11*, 2400104. [CrossRef]

14. Wang, J.; Zhang, H.; Nian, Y.; Chen, Y.; Cheng, H.; Yang, C.; Han, Y.; Tan, X.; Ye, J.; Yu, T. Disruption symmetric crystal structure favoring photocatalytic CO_2 reduction: Reduced* COOH formation energy barrier on Al doped CuS/TiO_2. *Adv. Funct. Mater.* **2024**, *34*, 2406549. [CrossRef]
15. Wach, A.; Zou, X.; Wojtaszek, K.; Kayser, Y.; Garlisi, C.; Palmisano, G.; Sá, J.; Szlachetko, J. Towards understanding the TiO_2 doping at the surface and bulk. *X-Ray Spectrom.* **2023**, *52*, 261–268. [CrossRef]
16. Yang, S.; Lu, Q.; Wang, F.; Zhi, Y.; Chen, J.; Wang, Y.; Zhang, H.; Yin, H.; Sun, P.; Cao, W. S-scheme SnO/TiO_2 heterojunction with high hole mobility for boosting photocatalytic degradation of gaseous benzene. *Chem. Eng. J.* **2023**, *478*, 147345. [CrossRef]
17. Roy, P.; Vats, A.K.; Tang, L.; Kurokawa, Y.; Pandey, S.S. Controlling adsorption of two dyes on TiO_2 surface to improve the efficiency of see-through dye-sensitized solar cells. *Sol. Energy* **2024**, *269*, 112339. [CrossRef]
18. Schneider, J.; Matsuoka, M.; Takeuchi, M.; Zhang, J.; Horiuchi, Y.; Anpo, M.; Bahnemann, D.W. Understanding TiO_2 photocatalysis: Mechanisms and materials. *Chem. Rev.* **2014**, *114*, 9919–9986. [CrossRef] [PubMed]
19. Asahi, R.; Morikawa, T.; Irie, H.; Ohwaki, T. Nitrogen-doped titanium dioxide as visible-light-sensitive photocatalyst: Designs, developments, and prospects. *Chem. Rev.* **2014**, *114*, 9824–9852. [CrossRef] [PubMed]
20. Pookmanee, P.; Promwanna, K.; Sangsrichan, S.; Kitikul, J.; Thanomwat, M.; Chaiwoot, P.; Kruefu, V.; Ubolsook, P.; Jansanthea, P. Calcination-Free Hydrothermal Synthesis of Nitrogen-Doped TiO_2: Integrating Photocatalytic Performance and Life Cycle Assessment for Sustainable Water Treatment. *ChemistrySelect* **2025**, *10*, e03820. [CrossRef]
21. Teleki, A.; Wengeler, R.; Wengeler, L.; Nirschl, H.; Pratsinis, S. Distinguishing between aggregates and agglomerates of flame-made TiO_2 by high-pressure dispersion. *Powder Technol.* **2008**, *181*, 292–300. [CrossRef]
22. Faure, B.; Lindeløv, J.S.; Wahlberg, M.; Adkins, N.; Jackson, P.; Bergström, L. Spray drying of TiO_2 nanoparticles into redispersible granules. *Powder Technol.* **2010**, *203*, 384–388. [CrossRef]
23. Luna, M.; Mosquera, M.J.; Vidal, H.; Gatica, J.M. Au-TiO_2/SiO_2 photocatalysts for building materials: Self-cleaning and de-polluting performance. *Build. Environ.* **2019**, *164*, 106347. [CrossRef]
24. Seifi, A.; Salari, D.; Khataee, A.; Çoşut, B.; Arslan, L.Ç.; Niaei, A. Enhanced photocatalytic activity of highly transparent superhydrophilic doped TiO_2 thin films for improving the self-cleaning property of solar panel covers. *Ceram. Int.* **2023**, *49*, 1678–1689. [CrossRef]
25. Kignelman, G.; Eyley, S.; Zhou, C.; Tunca, B.; Gonon, M.; Lahem, D.; Seo, J.W.; Thielemans, W. Colloidal Stability and Aggregation Mechanism in Aqueous Suspensions of TiO_2 Nanoparticles Prepared by Sol–Gel Synthesis. *Langmuir* **2021**, *37*, 14846–14855. [CrossRef] [PubMed]
26. Jena, K.D.; Lim, K.; Xu, Y.; Sharma, N.; Cao, P. Enhancing Charge Storage of Anatase Nanoparticles through Pseudocapacitance in Amorphous–Crystalline–Amorphous Architectures. *ACS Appl. Energy Mater.* **2024**, *7*, 6908–6919. [CrossRef]
27. Ravikumar, M.P.; Adhigan, M.; Govindaraju; Rokhum, S.L.; Mohan, S. Structure-Property Relationship in Lightly and Heavily Gas-Phase N-Doped TiO_2 Nanoparticles for Solar-Driven Photocatalysis. *Chem.–Asian J.* **2025**, *20*, e70347. [CrossRef] [PubMed]
28. Dubey, R.S.; Jadkar, S.R.; Bhorde, A.B. Synthesis and characterization of various doped TiO_2 nanocrystals for dye-sensitized solar cells. *ACS Omega* **2021**, *6*, 3470–3482. [CrossRef] [PubMed]
29. Wang, J.; Yu, Y.; Li, S.; Guo, L.; Wang, E.; Cao, Y. Doping behavior of Zr^{4+} ions in Zr^{4+}-doped TiO_2 nanoparticles. *J. Phys. Chem. C* **2013**, *117*, 27120–27126. [CrossRef]
30. Lu, W.; Zhu, H.; Birmingham, B.; Craft, N.; Hu, J.; Park, K.; Zhang, Z. Phase transition of individual anatase TiO_2 microcrystals with large percentage of (001) facets: A Raman mapping and SEM study. *Phys. Chem. Chem. Phys.* **2023**, *25*, 3199–3210. [CrossRef] [PubMed]
31. Alhomoudi, I.A.; Newaz, G. Residual stresses and Raman shift relation in anatase TiO_2 thin film. *Thin Solid Films* **2009**, *517*, 4372–4378. [CrossRef]
32. Xue, X.; Ji, W.; Mao, Z.; Mao, H.; Wang, Y.; Wang, X.; Ruan, W.; Zhao, B.; Lombardi, J.R. Raman investigation of nanosized TiO_2: Effect of crystallite size and quantum confinement. *J. Phys. Chem. C* **2012**, *116*, 8792–8797. [CrossRef]
33. Zhu, K.-R.; Zhang, M.-S.; Chen, Q.; Yin, Z. Size and phonon-confinement effects on low-frequency Raman mode of anatase TiO_2 nanocrystal. *Phys. Lett. A* **2005**, *340*, 220–227. [CrossRef]
34. Yalçın, Y.; Kılıç, M.; Çınar, Z. The role of non-metal doping in TiO_2 photocatalysis. *J. Adv. Oxid. Technol.* **2010**, *13*, 281–296. [CrossRef]
35. Tong, Q.; Cai, T.; Yuan, J.; He, D. Enhanced visible-light activation of persulfate for the removal of RhB by supported nano-(C, N, B)-tridoped TiO_2/copper foam mixed-crystals. *Environ. Sci. Pollut. Res.* **2024**, *31*, 1964–1979. [CrossRef] [PubMed]
36. Suwannaruang, T.; Kidkhunthod, P.; Chanlek, N.; Soontaranon, S.; Wantala, K. High anatase purity of nitrogen-doped TiO_2 nanorice particles for the photocatalytic treatment activity of pharmaceutical wastewater. *Appl. Surf. Sci.* **2019**, *478*, 1–14. [CrossRef]
37. Han, X.; Wang, X.; Xie, S.; Kuang, Q.; Ouyang, J.; Xie, Z.; Zheng, L. Carbonate ions-assisted syntheses of anatase TiO_2 nanoparticles exposed with high energy (001) facets. *Rsc Adv.* **2012**, *2*, 3251–3253. [CrossRef]

38. Liu, Y.; Lan, T.; Zhang, W.; Ding, X.; Wei, M. Hierarchically porous anatase TiO_2 microspheres composed of tiny octahedra with enhanced electrochemical properties in lithium-ion batteries. *J. Mater. Chem. A* **2014**, *2*, 20133–20138. [CrossRef]
39. Li, M.; Li, S.; Li, Y.; Li, X.; Yang, G.; Li, M.; Xie, Y.; Su, W.; Wu, J.; Jia, L.; et al. Cationic liposomes co-deliver chemotherapeutics and siRNA for the treatment of breast cancer. *Eur. J. Med. Chem.* **2022**, *233*, 114198. [CrossRef] [PubMed]
40. Song, S.H.; Lee, K.M.; Kang, J.B.; Lee, S.G.; Kang, M.J.; Choi, Y.W. Improved skin delivery of voriconazole with a nanostructured lipid carrier-based hydrogel formulation. *Chem. Pharm. Bull.* **2014**, *62*, 793–798. [CrossRef] [PubMed]
41. Kuznetsova, Y.V.; Rempel, A. Size and zeta potential of CdS nanoparticles in stable aqueous solution of EDTA and NaCl. *Inorg. Mater.* **2015**, *51*, 215–219. [CrossRef]
42. Saini, S.; Rawat, D.S.; Malik, R.; Kumar, S.; Kumar, S.; Meena, J. Synthesis of novel acryloyloxy tamarind kernel-TiO_2 nanocomposite film for photocatalytic removal of dye and UV absorption. *J. Chem. Sci.* **2026**, *138*, 18. [CrossRef]
43. Ghosh, S.; Imboon, T.; Layek, R.; Salunke, G.; Parihar, V.S.; Khumphon, J.; Webster, T.J.; Sutar, S.; Kityakarn, S.; Issro, C.; et al. Catechin-capped silver-doped titanium dioxide nanoparticle enhanced photocatalytic toxic dye degradation. *Front. Chem.* **2025**, *13*, 1576504. [CrossRef] [PubMed]
44. Pochapski, D.J.; Carvalho dos Santos, C.; Leite, G.W.; Pulcinelli, S.H.; Santilli, C.V. Zeta potential and colloidal stability predictions for inorganic nanoparticle dispersions: Effects of experimental conditions and electrokinetic models on the interpretation of results. *Langmuir* **2021**, *37*, 13379–13389. [CrossRef] [PubMed]
45. Han, R.; Liu, Y.; Mo, Y.; Xu, H.; Yang, Z.; Bao, R.; Pan, C. High anti-jamming flexible capacitive pressure sensors based on core–shell structured AgNWs@ TiO_2. *Adv. Funct. Mater.* **2023**, *33*, 2305531. [CrossRef]
46. Ray, S.C.; Mishra, D.K.; Panda, A.B.; Wang, H.; Bhattacharya, S.; Pong, W. Temperature-dependent electronic structure of TiO_2 thin film deposited by the radio frequency reactive magnetron sputtering technique: X ray absorption near-edge structure and X ray photoelectron spectroscopy. *J. Phys. Chem. C* **2022**, *126*, 8947–8952. [CrossRef]
47. Kongsong, P.; Taleb, A.; Masae, M.; Jeenarong, A.; Hansud, P.; Khumruean, S. Effect of nitrogen doping on the photocatalytic activity and hydrophobic property of rutile TiO_2 nanorods array. *Surf. Interface Anal.* **2018**, *50*, 1271–1277. [CrossRef]
48. Ren, Y.; Luan, R.; Zhao, Z.; Tang, L.; Wang, C.; Li, Y.; Li, M. Synthesis and Characterization of Se^{4+}@ TiO_2/PET Composite Photocatalysts with Enhanced Photocatalytic Activity by Simulated Solar Irradiation and Antibacterial Properties. *Molecules* **2025**, *30*, 1306. [CrossRef] [PubMed]
49. Gu, A.; Qiu, X.; Zhang, R.; Tang, W.; Zou, Q.; Liu, Y.; Yu, Z. Enhanced photochemical stability of hydrophobic TiO_2 via covalently anchoring near-monolayer octadecyl brushes and its robust superhydrophobic photocatalytic coatings. *Mater. Des.* **2026**, *267*, 116398. [CrossRef]
50. Sidor, K.; Lehmann, R.; Rokicińska, A.; Berniak, T.; Dębosz, M.; Kuśtrowski, P. Effect of decoration of C@TiO_2 core-shell composites with nano-Ag particles on photocatalytic activity in 4-nitrophenol degradation. *Catalysts* **2023**, *13*, 764. [CrossRef]
51. Cheng, X.; Yu, X.; Xing, Z. Characterization and mechanism analysis of N doped TiO_2 with visible light response and its enhanced visible activity. *Appl. Surf. Sci.* **2012**, *258*, 3244–3248. [CrossRef]
52. Alshehri, A.H.; Nelson-Fitzpatrick, N.; Ibrahim, K.H.; Mistry, K.; Yavuz, M.; Musselman, K.P. Simple plasma assisted atomic layer deposition technique for high substitutional nitrogen doping of TiO_2. *J. Vac. Sci. Technol. A* **2018**, *36*, 031602. [CrossRef]
53. Duan, Y.; Yang, Y.; Pang, X.; Li, S.; Wang, D.; Zhu, L.; Liang, C.; Sang, Y.; Yu, L. Efficient and durable photocatalytic degradation of benzene by interfacial electron redistribution induced by surface hydroxyl groups on PtOx/TiO_2. *Appl. Surf. Sci.* **2026**, *731*, 166432. [CrossRef]
54. Liu, X.; Chen, W.; Wang, W. F–Serve as Surface Trapping Sites to Promote the Charge Separation and Transfer of TiO_2. *ACS Omega* **2021**, *6*, 35799–35809. [CrossRef] [PubMed]
55. Anucha, C.B.; Bacaksiz, E.; Stathopoulos, V.N.; Pandis, P.K.; Argirusis, C.; Andreouli, C.-D.; Tatoudi, Z.; Altin, I. Preparation and characterization of supported molybdenum doped TiO_2 on α-Al_2O_3 ceramic substrate for the photocatalytic degradation of ibuprofen (IBU) under UV irradiation. *Catalysts* **2022**, *12*, 562. [CrossRef]
56. Xu, X.; Lai, L.; Jiang, J.; He, Z.; Song, S. C, N-codoped TiO2 with a nitrogen-doped carbon coating derived from 2, 6-diaminopyridine for visible light-induced photocatalytic hydrogen evolution. *J. Phys. Chem. C* **2019**, *123*, 9702–9712. [CrossRef]
57. Makuła, P.; Pacia, M.; Macyk, W. How to correctly determine the band gap energy of modified semiconductor photocatalysts based on UV–Vis spectra. *J. Phys. Chem. Lett.* **2018**, *9*, 6814–6817. [CrossRef] [PubMed]
58. Zhong, H.; Pan, F.; Yue, S.; Qin, C.; Hadjiev, V.; Tian, F.; Liu, X.; Lin, F.; Wang, Z.; Bao, J. Idealizing Tauc plot for accurate bandgap determination of semiconductor with ultraviolet–visible spectroscopy: A case study for cubic boron arsenide. *J. Phys. Chem. Lett.* **2023**, *14*, 6702–6708. [CrossRef] [PubMed]
59. Yang, T.; Zhao, Y.; Zuo, Y.; Chai, J.; Chen, Z.; Wong, L.M.; Bao, T.; Wang, S.; Jin, Y.J.; Yang, M. Incorporating nitrogen atoms at TiO_2 lattice sites for improved transparency and visible-light photocatalytic activity. *J. Phys. Chem. C* **2023**, *127*, 15271–15277. [CrossRef]

60. Xi, Q.; Papaefthimiou, V.; Le Breton, N.; Lenertz, M.; Takashima, M.; Keller, V.; Vileno, B.; Cottineau, T. Influence of nitridation conditions on the doping sites and photocatalytic visible light activity of Nb, N-codoped TiO_2. *Chem. Mater.* **2024**, *36*, 3705–3716. [CrossRef]
61. Huang, L.; He, G.; Yuan, Y.; Zhang, T.C.; Wang, Y.; Yuan, S. Trivalent metal ions (Al, Ga, In)-doped TiO_2 for enhanced photocatalytic desulfurization of H_2S: Band structure regulation, performance, and mechanism. *Ind. Eng. Chem. Res.* **2024**, *63*, 7154–7165. [CrossRef]
62. Wang, S.; Meng, K.; Zhao, L.; Jiang, Q.; Lian, J. Superhydrophilic Cu-doped TiO_2 thin film for solar-driven photocatalysis. *Ceram. Int.* **2014**, *40*, 5107–5110. [CrossRef]
63. Ahmad, A.A.; Alakhras, L.A.; Al-Bataineh, Q.M.; Telfah, A. Impact of metal doping on the physical characteristics of anatase titanium dioxide (TiO_2) films. *J. Mater. Sci. Mater. Electron.* **2023**, *34*, 1552. [CrossRef]
64. Zhang, J.; Li, L.; Li, H. Adsorption-controlled wettability and self-cleaning of TiO_2. *Langmuir* **2023**, *39*, 6188–6200. [CrossRef] [PubMed]
65. Deshpande, R.A.; Navne, J.; Adelmark, M.V.; Shkondin, E.; Crovetto, A.; Hansen, O.; Bachmann, J.; Taboryski, R. Understanding the light induced hydrophilicity of metal-oxide thin films. *Nat. Commun.* **2024**, *15*, 124. [CrossRef] [PubMed]
66. Han, F.; Zhu, L.; Huang, Z.; Zhou, Z. Photoinduced superhydrophilicity of anatase TiO_2 surface uncovered by first-principles molecular dynamics. *J. Phys. Chem. Lett.* **2020**, *11*, 7590–7594. [CrossRef] [PubMed]
67. Yang, Y.; Sun, T.; Ma, F.; Huang, L.-F.; Zeng, Z. Superhydrophilic Fe^{3+} doped TiO_2 films with long-lasting antifogging performance. *ACS Appl. Mater. Interfaces* **2021**, *13*, 3377–3386. [CrossRef] [PubMed]
68. Manrique-Holguin, M.; Alvear-Daza, J.J.; Murillo Sierra, J.C.; Irvicelli, K.G.; Canneva, A.; Donadelli, J.A.; Valencia, H.A.; Melin, V.; Campos, C.H.; Torres, C.C.; et al. Visible Light Absorption Is Not Always Related to N-Doped TiO_2 and High Photocatalytic Activity in Materials Synthesized by the Sol–Gel Method Using Urea and Ammonia as Precursors. *J. Phys. Chem. C* **2024**, *128*, 5597–5610. [CrossRef]
69. Kwon, J.; Choi, K.; Schreck, M.; Liu, T.; Tervoort, E.; Niederberger, M. Gas-phase nitrogen doping of monolithic TiO_2 nanoparticle-based aerogels for efficient visible light-driven photocatalytic H_2 production. *ACS Appl. Mater. Interfaces* **2021**, *13*, 53691–53701. [CrossRef] [PubMed]
70. Yang, F.; Wang, C.; Li, L.; Diao, H.; Wang, Y.; Zheng, X.; Li, C. Nickel-Doped TiO_2 nanoplate synthesized via mechanical ball Milling-Assisted Sol–Gel method for photocatalytic degradation of MB and NO. *Processes* **2025**, *13*, 1192. [CrossRef]
71. Sun, P.; Han, S.; Liu, J.; Zhang, J.; Yang, S.; Wang, F.; Liu, W.; Yin, S.; Ning, Z.; Cao, W. Introducing oxygen vacancies in TiO_2 lattice through trivalent iron to enhance the photocatalytic removal of indoor NO. *Int. J. Miner. Metall. Mater.* **2023**, *30*, 2025–2035. [CrossRef]
72. Huang, J.; Dou, L.; Li, J.; Zhong, J.; Li, M.; Wang, T. Excellent visible light responsive photocatalytic behavior of N-doped TiO_2 toward decontamination of organic pollutants. *J. Hazard. Mater.* **2021**, *403*, 123857. [CrossRef] [PubMed]
73. Krivtsov, I.; Ilkaeva, M.; Salas-Colera, E.; Amghouz, Z.; García, J.R.; Díaz, E.; Ordonez, S.; Villar-Rodil, S. Consequences of nitrogen doping and oxygen enrichment on titanium local order and photocatalytic performance of TiO_2 anatase. *J. Phys. Chem. C* **2017**, *121*, 6770–6780. [CrossRef]
74. Wang, H.; Du, Z.; Sun, Y.; Wang, H.; Ni, J.; Ni, C. Enhancing the surface N in TiO_2 using TiN as precursor for efficient photocatalytic NO removal and NO_2 suppression under visible light. *J. Environ. Chem. Eng.* **2025**, *13*, 120293. [CrossRef]
75. Le, T.P. Improvement in photocatalytic activity NOx using N-TiO2 photocatalytic materials under visible light. *Thu Dau Mot. Univ. J. Sci.* **2025**, *7*, 52–58. [CrossRef]
76. Khan, T.T.; Bari, G.A.R.; Kang, H.-J.; Lee, T.-G.; Park, J.-W.; Hwang, H.J.; Hossain, S.M.; Mun, J.S.; Suzuki, N.; Fujishima, A.; et al. Synthesis of N-doped TiO_2 for efficient photocatalytic degradation of atmospheric NOx. *Catalysts* **2021**, *11*, 109. [CrossRef]
77. Ai, Z.; Zhu, L.; Lee, S.; Zhang, L. NO treated TiO_2 as an efficient visible light photocatalyst for NO removal. *J. Hazard. Mater.* **2011**, *192*, 361–367. [CrossRef] [PubMed]
78. Todorova, N.; Vaimakis, T.; Petrakis, D.; Hishita, S.; Boukos, N.; Giannakopoulou, T.; Giannouri, M.; Antiohos, S.; Papageorgiou, D.; Chaniotakis, E.; et al. N and N, S-doped TiO_2 photocatalysts and their activity in NOx oxidation. *Catal. Today* **2013**, *209*, 41–46. [CrossRef]
79. Shang, H.; Li, M.; Li, H.; Huang, S.; Mao, C.; Ai, Z.; Zhang, L. Oxygen vacancies promoted the selective photocatalytic removal of NO with blue TiO_2 via simultaneous molecular oxygen activation and photogenerated hole annihilation. *Environ. Sci. Technol.* **2019**, *53*, 6444–6453. [CrossRef] [PubMed]
80. Gu, Z.; Cui, Z.; Wang, Z.; Qin, K.S.; Asakura, Y.; Hasegawa, T.; Hongo, K.; Maezono, R.; Yin, S. Intrinsic carbon-doping induced synthesis of oxygen vacancies-mediated TiO_2 nanocrystals: Enhanced photocatalytic NO removal performance and mechanism. *J. Catal.* **2021**, *393*, 179–189. [CrossRef]
81. Duan, Y.; Luo, J.; Zhou, S.; Mao, X.; Shah, M.W.; Wang, F.; Chen, Z.; Wang, C. TiO_2-supported Ag nanoclusters with enhanced visible light activity for the photocatalytic removal of NO. *Appl. Catal. B Environ.* **2018**, *234*, 206–212. [CrossRef]

82. Huang, Y.; Wang, P.; Wang, Z.; Rao, Y.; Cao, J.-J.; Pu, S.; Ho, W.; Lee, S.C. Protonated g-C_3N_4/Ti^{3+} self-doped TiO_2 nanocomposite films: Room-temperature preparation, hydrophilicity, and application for photocatalytic NO_x removal. *Appl. Catal. B Environ.* **2019**, *240*, 122–131. [CrossRef]
83. Li, S.; Zhu, G.; Jia, Y.; Pan, L.; Nie, J.; Rao, F.; Gao, J.; Zhang, F.; Kwon, N.; Liu, C. TiO_2 with exposed (001) facets/$Bi_4O_5Br_2$ nanosheets heterojunction with enhanced photocatalytic for NO removal. *Nanotechnology* **2020**, *31*, 254002. [CrossRef] [PubMed]

Disclaimer/Publisher's Note: The statements, opinions and data contained in all publications are solely those of the individual author(s) and contributor(s) and not of MDPI and/or the editor(s). MDPI and/or the editor(s) disclaim responsibility for any injury to people or property resulting from any ideas, methods, instructions or products referred to in the content.